

An imaging X-ray polarimeter for the study of galactic and extragalactic X-ray sources

Martin C. Weisskopf^{*a}, Ronaldo Bellazzini^b, Enrico Costa^c, Brian D. Ramsey^a,
Stephen L. O'Dell^a, Ronald F. Elsner^a, Allyn F. Tennant^a, George G. Pavlov^d, Giorgio Matt^e,
Victoria M. Kaspi^f, Paolo S. Coppi^g, Kinwah Wu^h, Oswald H. W. Siegmundⁱ, Vyacheslav E. Zavlin^j

^aNASA Marshall Space Flight Center (MSFC), Huntsville, AL, USA

^bIstituto Nazionale di Fisica Nucleare (INFN), Pisa, Italy

^cIstituto di Astrofisica Spaziale e Fisica Cosmica (IASF), Rome, Italy

^dPennsylvania State University, Astronomy & Astrophysics, University Park, PA, USA

^eUniversità degli Studi Roma Tre, Dipartimento di Fisica, Rome, Italy

^fMcGill University, Department of Physics, Montreal, QC, Canada

^gYale University, Department of Astronomy, New Haven, CT, USA

^hUniversity College London, Mullard Space Science Laboratory (MSSL), Holmbury St Mary, UK

ⁱUniversity of California Berkeley, Space Sciences Laboratory, Berkeley, CA, USA

^jUniversities Space Research Association (USRA), MSFC, Huntsville, AL, USA

ABSTRACT

Technical progress in X-ray optics and in polarization-sensitive X-ray detectors, which our groups pioneered, enables a scientifically powerful, dedicated space mission for imaging X-ray polarimetry. This mission is sufficiently sensitive to measure X-ray (linear) polarization for a broad range of cosmic sources—primarily those involving neutron stars, stellar black holes, and supermassive black holes (active galactic nuclei). We describe the technical basis, the mission concept, and the physical and astrophysical questions such a mission would address.

Keywords: X-ray astronomy, X-ray polarimetry, polarization-sensitive detectors, imaging detectors, X-ray optics

1. INTRODUCTION

The objective of the Imaging X-ray Polarimetry Explorer (*IXPE*) is to transform our understanding of the most energetic and exotic cosmic objects—neutron stars and black holes. To do this, *IXPE* will measure the X-ray linear polarization as a function of energy, time, and (where relevant) position. As the first dedicated X-ray-polarimetry observatory, *IXPE* will add a new dimension to X-ray astrophysics, significantly enlarging the observational phase space and addressing fundamental questions concerning high densities, high temperatures, non-thermal particles, strong magnetic and electric fields, and strong gravity effects. For example, “How do pulsars pulse?” “How fast do black holes spin?” “What is the physics of magnetars?” “What are the geometries and exactly how X rays are produced in quasars and X-ray binaries?”

***IXPE* is ideally suited for a small satellite program.** Progress in X-ray polarimetry requires a dedicated mission. Both the technology and the theoretical framework are sufficiently mature to make *IXPE* (Figure 1) a powerful astrophysical probe, which complements all current and planned X-ray missions.

***IXPE* is uncomplicated.** It uses 3 identical nickel-replicated grazing-incidence X-ray telescopes—similar to those MSFC builds and flies as balloon payloads. Each telescope focuses X rays into a proportional counter designed to track the path of the photo-ejected electron in the detector gas. The signature of linear polarization lies in the distribution of the electron-track initial direction—aligned to the incident X ray’s electric field. We first suggested exploiting full electron tracking for X-ray astronomical polarimetry and developed the technology and detector to be used on *IXPE*. The dimensions, mass, power, and telemetry requirements are well within current spacecraft capabilities and the mission is straightforward: A launch vehicle (e.g., Pegasus XL) can place *IXPE* into a low earth orbit (LEO).

* martin.c.weisskopf@nasa.gov; +1-256-961-7798; NASA/MSFC/VP62, 320 Sparkman Drive, Huntsville AL 35805-1912, USA.

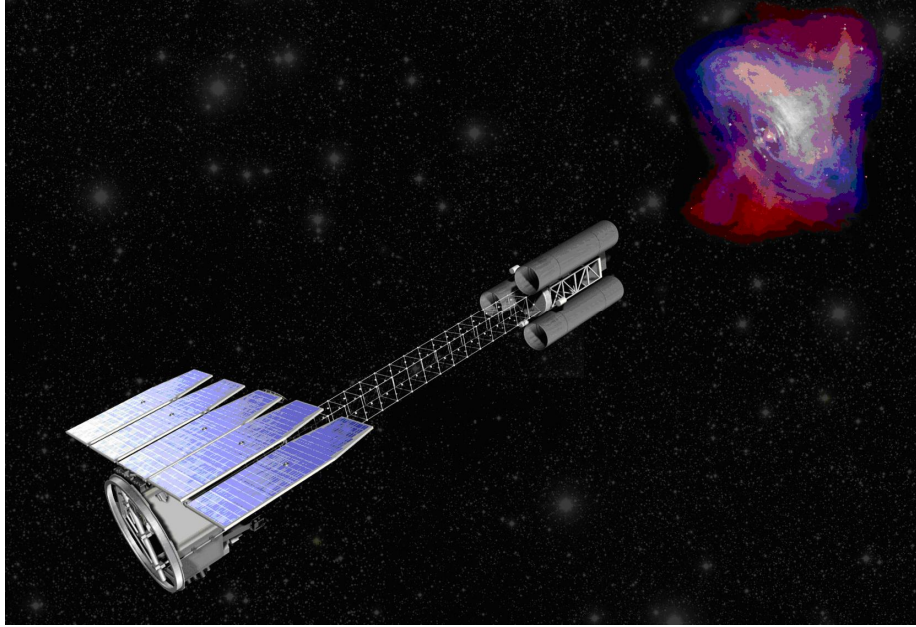


Figure 1—Artist's rendering of the design concept for the Imaging X-ray Polarimetry Explorer (*IXPE*).

2. THE SCIENCE

Only a few experiments have conducted X-ray polarimetry of cosmic sources. In rocket observations, we measured X-ray polarization from the Crab Nebula. The X-ray polarimeter that we designed and built for the Orbiting Solar Observatory (OSO-8), confirmed this result at 19 sigma ($P = 19.2\% \pm 1.0\%$), proving the synchrotron origin of the X-ray emission from this plerionic supernova remnant. Since our early experiments, polarimetry has remained a goal of X-ray astronomy due to the unique data it affords: The HEAO-2 (*Einstein Observatory*) and the Advanced X-ray Astrophysics Facility (*Chandra X-ray Observatory*) reference payloads each included an X-ray polarimeter prior to de-scoping. X-ray polarimetry is capable of providing a powerful tool for discriminating amongst models and understanding the nature of the sources and the physical processes. Here we give a brief overview of the theoretical basis for X-ray polarimetry and discuss a few examples.

2.1 Theoretical considerations

One expects polarized X rays from regions of ordered magnetic fields or aspheric matter distributions. Further, quantum or general relativistic effects in a strong magnetic or gravitational field affect the propagation of polarized radiation.

Ordered magnetic fields typically result in strongly polarized radiation. The degree and direction of polarization can depend upon photon energy, propagation effects, and magnetic-field strength and orientation. In the X-ray range, emission from nonrelativistic electrons is strongly polarized when the magnetic field exceeds about 10^{11} G—i.e., when the electron cyclotron frequency exceeds the photon frequency. Therefore, strongly magnetized neutron stars, such as magnetars, radio pulsars, and some accreting binaries are natural targets. For the most strongly magnetized, vacuum birefringence—a nonlinear quantum-electrodynamics effect—may also occur. In weaker magnetic fields, synchrotron radiation from ultrarelativistic electrons also produces highly-polarized radiation. Such sources include pulsar magnetospheres, pulsar-wind nebulae, and jets in active galactic nuclei (AGN) and in micro-quasars.

Aspheric matter distributions result in radiation polarized orthogonal to the scattering plane, even if the incident radiation is unpolarized. For example, this likely occurs in the Galactic Center, where X-ray polarimetry can uniquely test the hypothesis that the central supermassive black hole was active a few hundred years ago. Another example is X-ray emission from accretion disks, where radiation from deeper disk layers is scattered by electrons in the surface layers or in a hot corona. Disk accretion is common in sources like AGN and close X-ray binaries, where X-ray polarimetry will permit qualitatively new constraints on the geometry and physical properties of such systems. Scattering can also contribute to linear polarization of the X-ray emission of radio-loud AGN and Galactic microquasars, where softer photons Compton upscatter off an aspheric outflow—e.g., beam—of ultrarelativistic electrons.

General relativistic (GR) effects near a black hole—where space-time curvature is substantial—produce a special kind of anisotropy. Parallel transport along null geodesics and polarization rotation induced by the black-hole angular momentum (“gravitational Faraday rotation”) can modify the intrinsic polarization. Thus, polarimetry provides unique data to analyze these GR effects in the strong-field regime and to estimate the black-hole angular momentum. Such effects can be observed both in the Galactic black-hole binaries and supermassive black holes in AGN.

2.2 Magnetars

According to current thinking, superstrong (up to 10^{15} G) magnetic fields in some neutron stars power Soft Gamma-ray Repeaters (SGRs) and Anomalous X-Ray Pulsars (AXPs). In the magnetar model¹, low-level seismic activity in a superstrong magnetic field powers persistent emission through heating of the stellar interior, while large-scale crust fractures result in intense bursts^{2, 3}. In this model, thermal ($kT \approx 0.3\text{--}0.5$ keV) emission from the neutron star surface, likely upscattered via Compton scattering off relativistic particles in a twisted coronal magnetic field^{4, 5, 6}, could produce polarized persistent emission. Such polarization depends sensitively upon photon energy, magnetic-field strength and geometry, and rotational phase⁷. Figure 2 presents polarization light curves for a model of a hot polar cap⁸. These are the type of variations that *IXPE* may measure in order to constrain the basic physical properties of magnetars. *IXPE* can easily perform such measurements for the brightest persistent AXPs. For instance, *IXPE* can detect 10% polarization (99% confidence) of 4U 0142+61 in each of 10 phase bins in a 2.4 day observation.

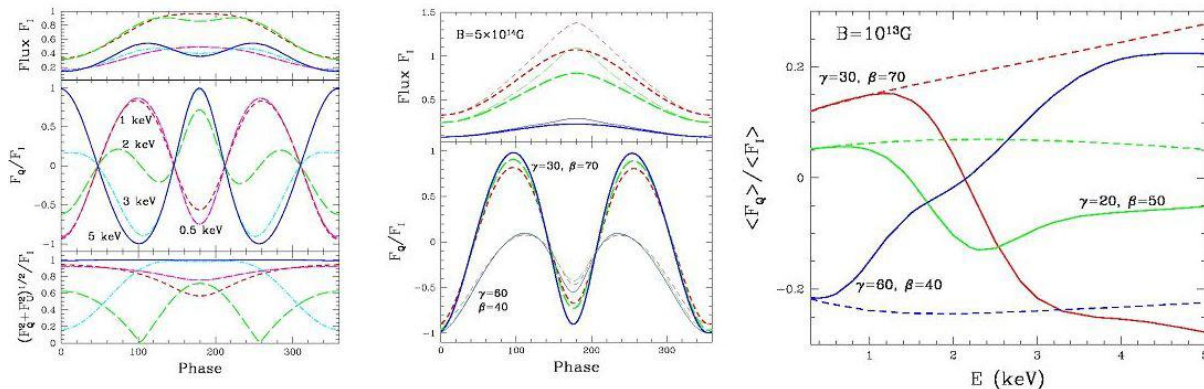


Figure 2—Phase dependence of the spectral flux, Stokes parameter F_Q/F_I , and polarization degree produced by the polar cap of a rotating neutron star with $kT = 0.43$ keV and $B = 10^{13}$ G (left) and 5×10^{14} G (center) for different photon energies. The right panel shows the energy dependence of the phase-averaged polarization (positive and negative values corresponding to projection of the spin axis onto the celestial plane) for $B = 10^{13}$ G and different combinations of angles γ between the line-of-sight and the spin axis, and β between the spin and magnetic axes. The dashed curves denote results when vacuum polarization is ignored (adopted from Lai & Ho⁸).

The origin of magnetar outburst and subsequent decay remains uncertain: Plausible causes include twisting/untwisting of the magnetosphere⁹ or thermal relaxation following internal or external heat release¹⁰. Understanding outbursts and decays is important for identifying the origin of transient magnetars¹¹, key objects for establishing the magnetar birthrate. Given the frequency and duration of magnetar outbursts and their estimated number in the Galaxy, *IXPE* is likely to observe at least one such event in a one-year mission.

IXPE can also probe a QED effect—vacuum birefringence in strong magnetic fields—predicted 70 years ago¹², but not yet convincingly verified. The most vivid polarization signatures are a strong energy dependence of the Stokes parameter F_Q/F_I (Figure 2 right panel) and a 90° -position-angle jump at an energy-dependent phase, occurring where the normal-mode propagation through the so-called “vacuum resonance”¹³ changes from adiabatic to non-adiabatic¹⁴.

2.3 Radio pulsars

Radio pulsars are isolated, rotation-powered neutron stars, converting rotational energy to ultrarelativistic particles and radiation. Theoretical models predict high linear polarization varying with pulse phase. However, the physics of the emission—even its location (e.g., near the pulsar’s polar cap or in the magnetosphere)—remain unclear. X-ray polarimetry can provide decisive information to discriminate amongst models. For the Crab and Vela pulsars, an instrument such as *IXPE* will also be able to obtain spatially-resolved polarimetry of the pulsar, jets, and tori.

The origin of pulsar high-energy non-thermal radiation remains a key problem. Controversy persists over the site of this emission—directly above the polar cap, where the coherent radio pulses originate^{15, 16, 17, 18}; in the outer magnetosphere near the light cylinder^{19, 20, 21, 22}; or in the “slot gap”, along open magnetic field lines between the polar cap and the outer magnetosphere^{23, 24, 25}. As each of these models can approximately produce the observed intensity pulse shapes (even in the γ -ray regime), only polarimetry reliably discriminates amongst them (Figure 3). Optical polarimetry of the Crab pulsar^{26, 27} finds high (up to 35%) linear polarization, varying rapidly through each pulse component. While we might expect similar behavior in X rays, the phase dependence of the polarization angle may differ —e.g., due to angular and frequency dependences of the emitted radiation or to vacuum birefringence in the non-uniform, strong magnetic field²⁸. Thus, measuring the swing of the polarization across the pulse and comparing it with the optical will locate the sites of emission and probe the magnetospheric particle population. Our previous X-ray polarimetry of the Crab Nebula with OSO-8 could place only 20%-30% limits on the pulsar's polarization in large phase bins²⁹. In contrast, *IXPE*'s angular resolution ($< 30''$ half-power diameter, HPD), time (5- μ s) resolution, and collecting area enable sensitive measurement—e.g., 3% polarization (99% confidence) in each of 8 phase bins—of pulse and interpulse polarization sweeps.

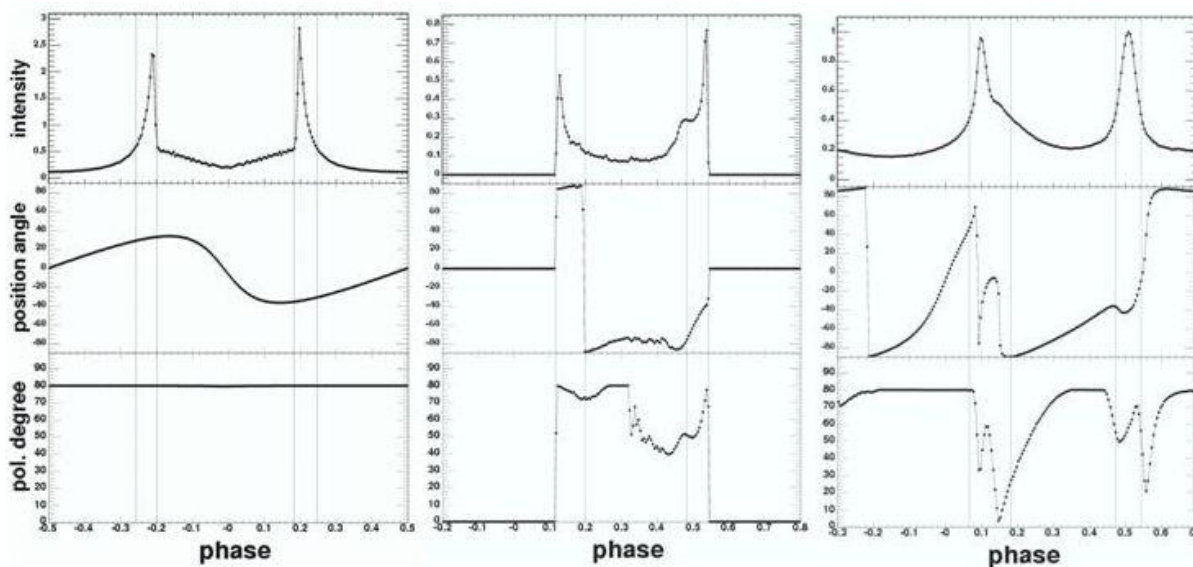


Figure 3—Intensity and polarization position angle and degree predicted for the polar-cap (left; Daugherty & Harding³⁰); outer-gap (middle; Romani & Yadigaroglu³¹), and slot-gap (right; Dyks et al.²⁵) models.

2.4 Pulsar-wind nebulae

Pulsar-wind nebulae (PWNe) are among the most spectacular targets of X-ray astronomy. Their X-ray emission is synchrotron radiation of the ultrarelativistic pulsar wind shocked in the ambient medium. As the polarization position angle is perpendicular to the magnetic-field direction at the site of emission, spatially resolved polarimetry will probe the magnetic-field topology and its connection with the PWNe morphology.

While radio^{32, 33} and optical^{34, 35} polarization maps have established the overall geometry of the magnetic field of the Crab PWNe, spatially resolved X-ray polarimetry can provide unique and crucial information on acceleration and cooling mechanisms. The need for such measurements is particularly clear following our spectacular high-resolution *Chandra* observations (Figure 4 right panel), which exhibited its complex morphology (including a torus and jets³⁶) and spatially dependent spectra³⁷. *IXPE* will easily be able to measure the polarization in a number of image elements, thus providing the first spatially resolved X-ray polarimetry of a PWNe. A 7.3-d observation has the sensitivity to detect well below 2% polarization (99% confidence) in each of 5 spatial bins, including one centered on the southeast jet. This estimate allows for the fact that 50% of the flux in the detect cell is from other regions and is thus a (polarized) background.

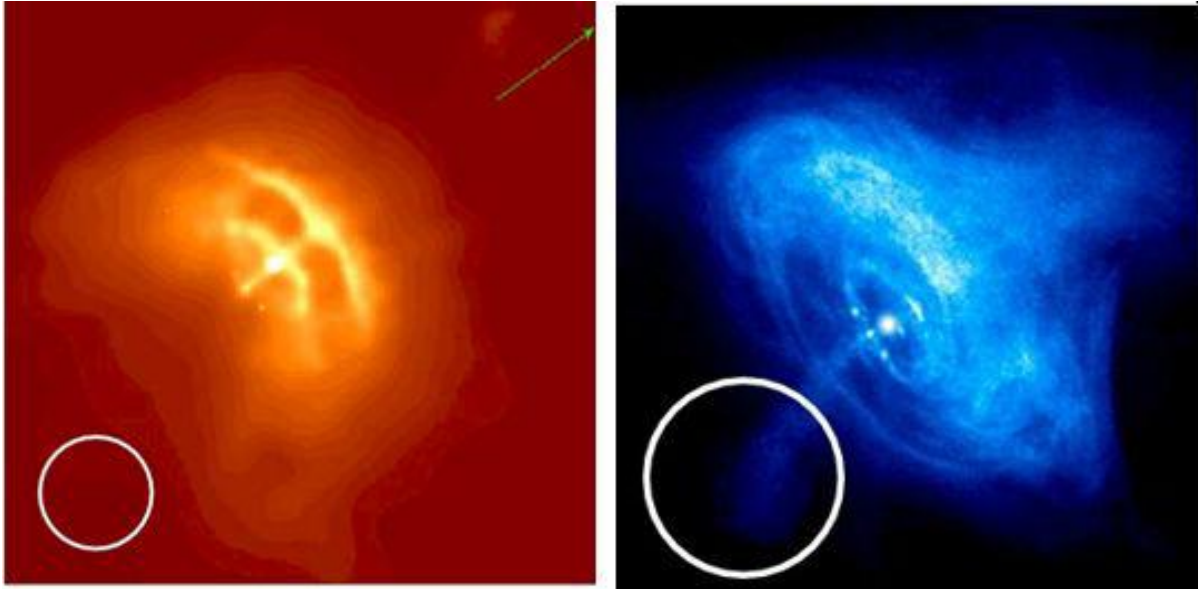


Figure 4—Chandra images of the Vela (left) and Crab (right) pulsar-wind nebulae (PWNe). The circle at the lower left of each image displays *IXPE*'s 30" half-power diameter (HPD).

2.5 Active Galactic Nuclei (AGN)

AGN convert the gravitational energy of material accreting onto a supermassive black hole into radiation and kinetic energy of outflowing matter, often including relativistic plasma. AGN can be classified radio-loud and radio-quiet. In radio-loud AGN, a relativistic, highly collimated jet is present; in the subclass blazars, the jet is directed close to the line-of-sight and, due to Doppler boosting, dominates the emission at all frequencies. The non-thermal emission generally comprises two emission components—synchrotron and Compton scattering—each of which is highly polarized. Thus, X-ray polarimetry will provide important information on X-ray emission mechanisms and geometry. For instance, in blazars, where the Compton peak dominates the X-ray emission, polarimetry will allow distinguishing between synchrotron-self-Compton³⁸ (SSC) and external Compton^{39,40} (EC) processes.

In non-blazar radio-loud AGN, the jet is not directed along the line-of-sight. Consequently, X-ray emission from the jet does not dominate that from the accretion disk or corona. X-ray polarimetry offers a way to separate these components. At least two sources—Centaurus A and 3C 273—are bright enough for *IXPE* to perform energy-dependent polarimetry down to a few percent in a few days.

Even in AGN without strong jets, non-spherical geometry of emitting (or scattering) regions tends to result in significant polarization. For example, thermal Comptonization of soft disk photons by electrons in a hot ($kT \approx 10^9$ K) corona may polarize X rays up to 10% or more^{41, 42, 43}. Similarly, X-ray emission reprocessed by the accretion disk—the Compton-reflection component—is also polarized up to 20%, depending upon inclination angle^{44, 45}. For the brightest sources, a few-day integration can detect a few-percent polarization. Some of these AGN (e.g., NGC 4151, IC 4329A, MCG-5-23-16) are obscured below about 2 keV, indicating according to the Unification Model⁴⁶ high inclinations and, hence, high degrees of polarization. Strong-field GR effects modify both primary emission and disk-reflection components^{47, 48, 49}. For instance, in the “*light-bending*” model proposed by Miniutti et al.⁵⁰ to explain the temporal behavior of MCG-6-30-15, we have shown⁵¹ that large variations of the polarization angle are expected when the reflection component dominates—i.e., when the primary source goes very close to the black hole—with net polarization up to 15%.

The few-million-solar-mass black hole in our own Galactic Center is currently exceptionally inactive, with a luminosity only 10^{-11} Eddington. However, the molecular cloud Sgr B2, at a projected distance of about 100 pc from the nucleus, shows a pure reflection spectrum indicating illumination from an external source. With no sufficiently bright illuminating sources present, Koyama et al.⁵² suggested that the X radiation from Sgr B2 is an echo of a past active phase of the central black hole. If correct, the reflected radiation must be polarized⁵³, with a position angle perpendicular to the direction of the illuminating photons. Therefore, *IXPE* can confirm or reject unambiguously the hypothesis that our Galaxy was a low-luminosity AGN in the recent past.

3. THE GAS PIXEL DETECTOR

We have designed, built, and flown both Bragg-crystal and scattering X-ray polarimeters in sounding rockets⁵⁴ and on OSO-8⁵⁵. We also played a major role in design, construction, and testing of the Stellar X-ray Polarimeter (SXP)^{56, 57}. However, narrow band pass, high detector background, and/or systematic effects limited the sensitivity of each device.

We have spent over 30 years overcoming the inadequacy of previous devices, culminating in the development of a new type of polarimeter—one based on the photoelectric effect, which dominates at low energies where source fluxes are typically high. This new polarimeter measures the anisotropy of the initial directions of photoelectrons to gauge the polarization state of X rays photoabsorbed in a gaseous medium.

In the photoelectric interaction, the photoelectron has an initial direction peaked (with a \cos^2 distribution) around the electric-field direction of the photon. This photoelectron slows through ionizing collisions with the surrounding material until it eventually stops. The resulting ionization string tracks the photoelectron's path, with the direction at the start of the track marking the initial direction of the photoejected electron. In practice, photoelectron tracks are quite short, so that gas-filled counters must have very fine spatial resolution to image the track sufficiently accurately. We originally demonstrated proof of principle for a gas-filled photoelectron-tracking detector using a CCD-based optical system to register light induced by the photoelectron track⁵⁸. More recently, our team has greatly refined this technique⁵⁹ by developing the Gas Pixel Detector (GPD) for X-ray polarimetry. When placed at the focus of our X-ray optics, this detector makes *IXPE* an extremely powerful polarimeter — two orders of magnitude more sensitive than that on OSO-8—thus opening the X-ray polarization window to sensitive scientific exploration.

Figure 5 illustrates the operation of a gas pixel proportional-counter detector. An incident X ray enters through a thin window and interacts in the detector fill gas—a mixture of low-Z components optimized for long tracks with little diffusion. The resulting ionization track then drifts toward the Gas Electron Multiplier (GEM), where each electron is multiplied and transferred to a pixel anode array for readout.

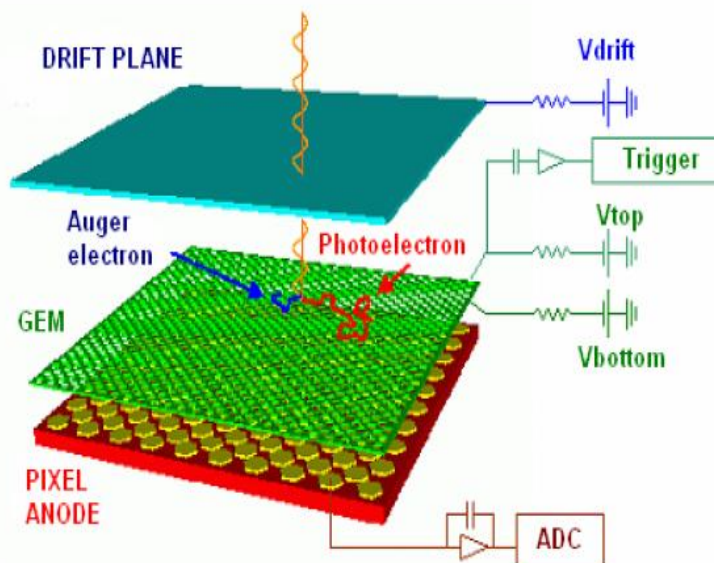


Figure 5—Schematic of the gas pixel detector, showing the polarization-dependent photoelectron's ionization track.

The heart of the detector is the pixel anode readout⁶⁰, a custom CMOS-based Application Specific Integrated Circuit (ASIC) that combines the functions of charge collection and readout electronics. Now in its third generation, this chip has a top metal layer patterned in a matrix of ($\approx 100,000$) 50- μm hexagonal pixels, which constitute a finely constructed collecting electrode. Each pixel is connected to a full electronic readout chain consisting of a charge-sensitive preamplifier, shaper, sample-and-hold, and multiplexing system. The equivalent charge noise level for each chain is about $50 e^-$ (1σ). For an effective amplification of 500, this enables resolving individual electrons in the photoelectron track at high signal to noise.

Figure 6 displays a schematic of the construction of the detector and a photograph of the prototype. An insulating case houses the assembly, which is bonded to the ASIC readout⁶¹. Oxford Instruments (formerly Metorex, Finland) assembles the detector, pumps and bakes it for a week, and then fills with the specified operating gas mixture before sealing it.

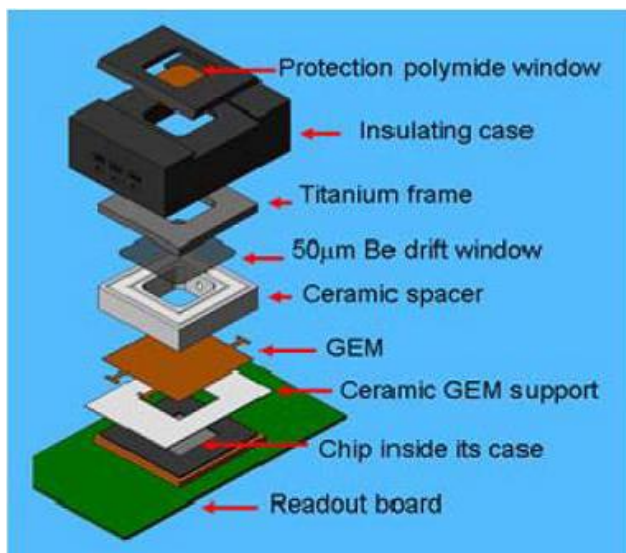


Figure 6—Illustration of the detector components (top) and photograph of the prototype detector (bottom).

Optimizing gas composition, operating pressure, and detector depth is a trade between absorption efficiency and track length⁶². Our recent studies found that a mixture of Dimethylether (DME) and Helium (80/20) at 1-atmosphere total pressure and 1-cm depth gives the best overall performance over 2–8 keV. Figure 7 shows a typical track with this mixture. The initial interaction point is to the left and the termination point, the bright blob, on the right. The challenge in extracting information is obvious: Most of the signal is at the end of the track, whereas the desired information on the photoelectron direction is at the beginning. We have developed sophisticated, experimentally-verified, software that reliably determines the initial interaction point and initial photoelectron direction with high fidelity. For 80% of all tracks studied, we obtain individual photoejection angles to within 20° (measured with a polarized signal) and locate the site of the initial interaction to within 100 µm (full-width half-maximum).

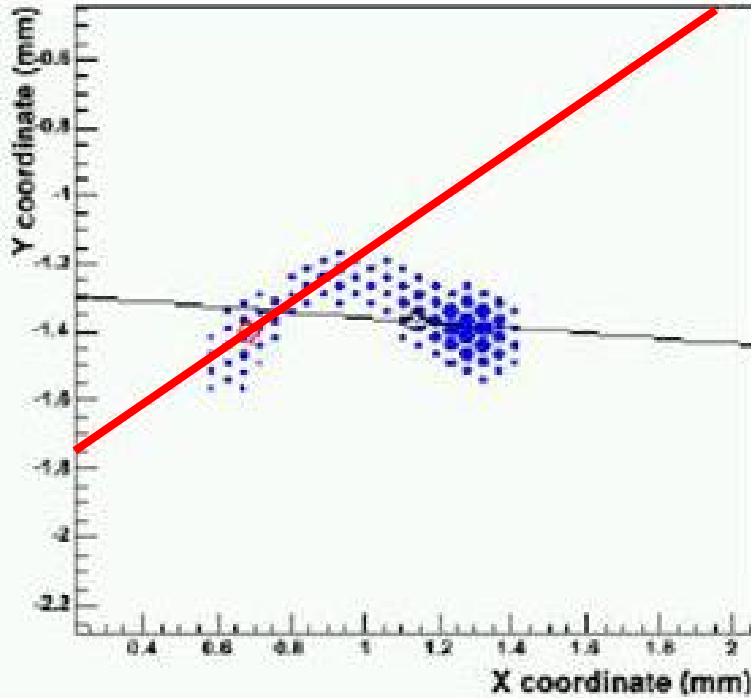


Figure 7—Electron track for a 6.4-keV photon. The thin (black) and thick (red) lines are the initial and final solutions, respectively, for the photoejection direction.

A key factor in determining the sensitivity of a polarimeter is the modulation factor, a measure of the variation of the initial photoelectron track direction for a 100% polarized input. With this gas mixture, pressure, and detector dimensions (Table 1), the modulation factor is very small below 2 keV (the effective threshold of the detector) where tracks are short and the angular distribution appears almost spherical, but it rises very quickly above this energy. For Table 1, note that the detector mass and power are for 1 detector.

Table 1—Detector parameters

Number of detectors	3 (1 per telescope)
Detector sensitive area	15 mm × 15 mm
Fill gas and pressure	He/DME (20/80) at 1 atm
Entrance window	50- μ m-thick beryllium
Absorption and drift region	10-mm deep
Peak detector efficiency and energy	24% @ 2 keV
GEM material	Gold-coated Kapton
GEM thickness	50 μ m
GEM hole pitch	50 μ m
Number of readout pixels	300 × 352
Readout hexagonal pitch	50 μ m
Detector mass	7.9 kg (per detector)
Detector power	5.7 W (per detector)

Equally important for any polarimeter is to verify that an unpolarized input signal produces no significant modulation, which could lead to false positives. Figure 8 shows the angular distribution for our detector irradiated with polarized (left panel) and with unpolarized (right panel) beams. For the unpolarized beam, we find no indication of false polarization, measuring a modulation of $0.18\% \pm 0.14\%$ —i.e., zero within the (3σ) uncertainty—that demonstrates that systematic effects are well under the 1% level.

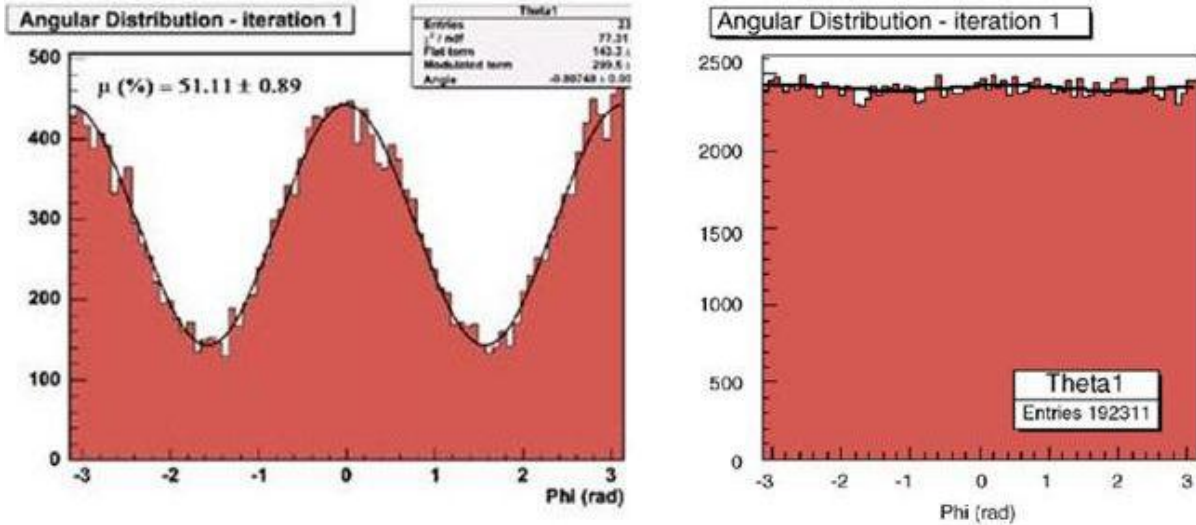


Figure 8—Measurements of the modulation for a 100%-polarized beam at 5.1 keV (left), and for an unpolarized beam at 5.9 keV (right). The measured amplitudes are 51% and 0.18%, respectively.

4. THE X-RAY OPTICS

In order to reduce background and to enable imaging polarimetry, each detector lies at the focus of an X-ray telescope. We shall build the telescopes using an electroformed-nickel replication process that we have been developing at MSFC since the early 1990s. The attraction of this approach is in-house fabrication and that it yields full-shell optics that typically exhibit an HPD of about 25". All the production facilities—polishing stations, plating baths, coating chambers, metrology equipment, etc.—used to produce X-ray telescopes for MSFC’s High Energy Replicated Optics (HERO) balloon payload^{63, 64} are available for use for *IXPE*. Table 2 summarizes the parameters characterizing the telescope. Note that the telescope effective area and mass are for 1 telescope.

Table 2—Telescope parameters

Number of telescopes	3
Shells per telescope	30
Focal length	4000 mm
Total shell length	600 mm (300 mm per surface)
Shell diameter	274 mm (outermost) 142 mm (innermost)
Shell thickness	224 μ m (outermost) 145 μ m (innermost)
Mean grazing angle	29.4' (outermost) 15.3' (innermost)
Shell material	Nickel–cobalt alloy
Telescope effective area	300 cm ² @ 2 keV (per telescope)
Angular resolution	<30" HPD
Detector-limited full FOV	18.9' \times 18.9'
Vignetting loss at edge of FOV	20%
Mirror mass	18.6 kg (per telescope)
Telescope mass (including mirrors)	27.5 kg (per telescope)

5. SENSITIVITY

The quantity most useful for assessing the performance of a polarimeter is the minimum detectable polarization (MDP) at 99% confidence:

$$\text{MDP}_{99\%} = (4.29 \times 10^2 \% / \mu) \sqrt{\frac{R_S + R_B}{R_S^2 t}},$$

where R_S and R_B are detected counting rates (in counts/s) for signal and background, t is the observation time and μ is the modulation factor, defined as the variation in the measured photoelectron emission angles for a 100% polarized beam in the absence of any background.

To derive source counting rates, we folded known source spectra with our system effective area (Figure 9), factoring in the telescope effective area (including thermal shielding), our detector efficiency (including a track-recognition efficiency of 0.8), and an encircled-energy efficiency (0.95). Based upon numerous satellite experiences, we assumed a detector (2–8 keV) background count rate per detector of 1.1×10^{-4} ct/s within a 700- μm radius.

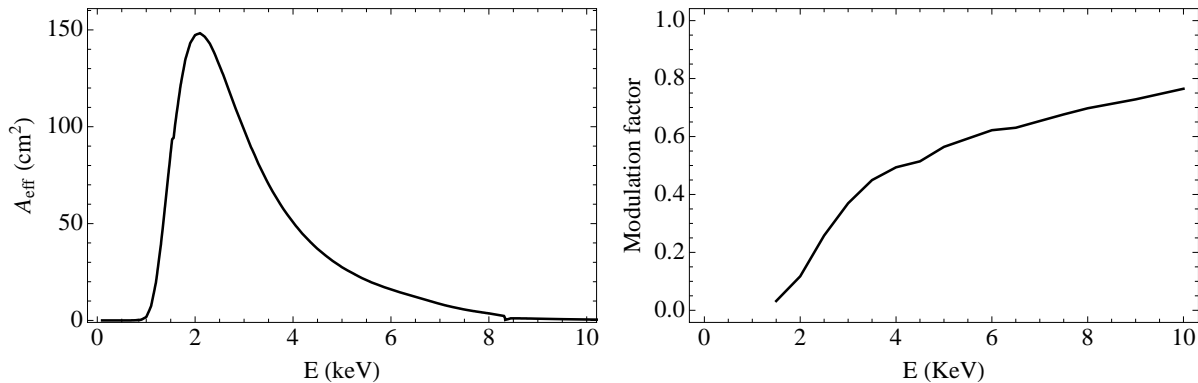


Figure 9—*IXPE* system (3 telescopes and detectors) net effective area (left) and modulation factor (right).

To obtain the modulation factor μ as a function of energy, we utilized data from test detectors measured at discrete energies and interpolated using data from high-fidelity simulations. Combining these, we obtain the 99%-confidence minimum detectable polarization $\text{MDP}_{99\%}$ as a function of source flux (in units of 10^{-11} ergs $\text{cm}^{-2} \text{s}^{-1}$, for photon indices between 1.4 and 2.1 and hydrogen column densities below 10^{22}cm^{-2}) and of integration time.

Figure 10 summarizes the results of these simulations, showing the integration time required to reach a specified $\text{MDP}_{99\%}$, as a function of source flux in the 2–8-keV band. For a given $\text{MDP}_{99\%}$, the closely spaced diagonal parallel lines bound the 1.4–2.1 range of photon indices. The labels adjacent to the dashed vertical lines give the number of sources from the HEASARC’s LMXB and HMXB catalogs, above various flux levels. The top axis shows the number of extragalactic sources (based upon the $\log N$ – $\log S$ relationship given by Moretti et al.⁶⁵) corresponding to the limiting flux on the bottom axis. The dashed (green) line near $F_{-11} = 2000$ marks the Crab-Nebula flux; the (green) dot indicates the time required by the OSO-8 polarimeter to achieve $\text{MDP}_{99\%} = 3\%$ for this flux. Finally, the (green) arrow depicts how *IXPE* can make the same measurement in 1% the time—i.e., a 2-order-of-magnitude improvement.

As Figure 10 demonstrates, *IXPE* is capable of obtaining scientifically meaningful X-ray polarization measurements of numerous cosmic sources, both Galactic and extragalactic. During the 6-month discovery phase of our design reference mission, *IXPE* would observe over 40 targets—including 4 pulsar-wind nebulae (PWNe), 4 other pulsars, 12 low-mass X-ray binaries (LMXB), 6 high-mass X-ray binaries (HMXB), 8 blazars, and 6 other active galactic nuclei (AGN). For a 1-year mission, this allows another 6 months for more detailed investigation of surveyed targets. Such follow-up observations will study the dependence of detected polarization upon photon energy and/or time (e.g., pulse phase).

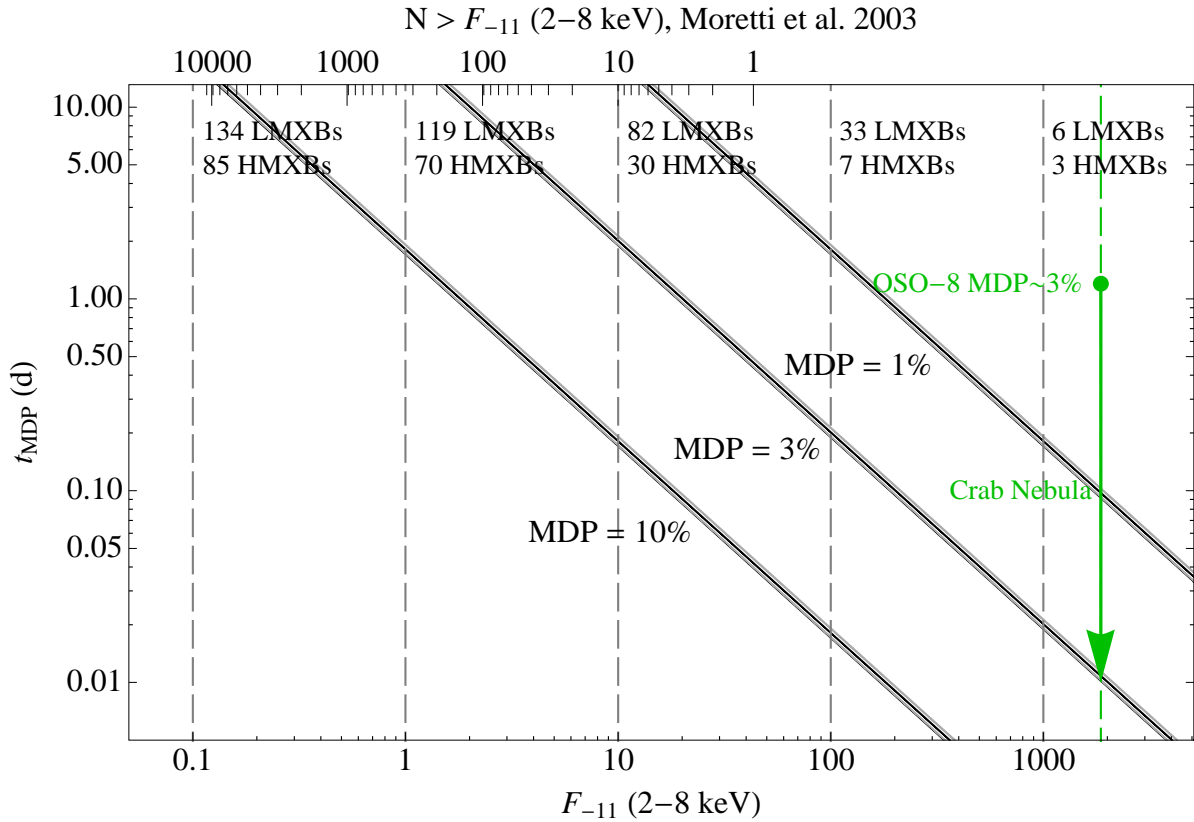


Figure 10—IXPE polarization sensitivity. The plot displays the integration time (in days) to reach a given $\text{MDP}_{99\%}$, as a function of 2–8-keV source flux (in $10^{-11} \text{ ergs cm}^{-2} \text{ s}^{-1}$). See text for details.

REFERENCES

- ¹ Duncan, R., & Thompson, C., *ApJ* **392**, L9 (1992).
- ² Thompson, C., & Duncan, R., *MNRAS* **275**, 255 (1995).
- ³ Thompson, C., & Duncan, R., *ApJ* **473**, 322 (1996).
- ⁴ Thompson, C., Lyutikov, M., & Kulkarni, S., *ApJ* **574**, 332 (2002).
- ⁵ Fernandez, R., & Thompson, C., *ApJ* **660**, 615 (2007).
- ⁶ Guver, T., Ozel, F., Gogus, E., & Kouveliotou, C., *ApJ* **667**, L73 (2007).
- ⁷ Pavlov, G.G., & Zavlin, V.E., *ApJ* **529**, 985 (2000).
- ⁸ Lai, D., & Ho, W.C.G., *PhRvL* **91**, 071101 (2003).
- ⁹ Thompson, C., Lyutikov, M., & Kulkarni, S., *ApJ* **574**, 332 (2002).
- ¹⁰ Guver, T., Ozel, F., Gogus, E., & Kouveliotou, C., *ApJ* **667**, L73 (2007).
- ¹¹ Ibrahim, A. I., Markwardt, C. B., Swank, J. H., Ransom, S., Roberts, M., Kaspi, V., Woods, P. M., Safi-Harb, S., Balman, S., Parke, W. C., Kouveliotou, C., Hurley, K., & Cline, T., *ApJ* **609**, 211 (2004).
- ¹² Heisenberg, W., & Euler, H., *ZPhy* **38**, 714 (1936).
- ¹³ Pavlov, G.G., & Shibano, Yu.A., *ZhETF* **76**, 1457 (1979).
- ¹⁴ Pavlov, G.G., & Gnedin, Yu. N., *ASPRv* **3**, 187 (1984).
- ¹⁵ Ruderman, M.A., & Sutherland, P.G., *ApJ* **196**, 51 (1975).
- ¹⁶ Arons, J., & Scharlemann, E.T., *ApJ* **231**, 854 (1979).
- ¹⁷ Daugherty, J.K., & Harding, A.K., *ApJ* **252**, 337 (1982).
- ¹⁸ Harding, A.K., & Muslimov, G.A., *ApJ* **508**, 328 (1998).
- ¹⁹ Cheng, K. S., Ho, C., & Ruderman, M., *ApJ* **300**, 522 (1986).

-
- ²⁰ Romani, R.W., *ApJ* **470**, 469 (1996).
- ²¹ Zhang, L., Cheng, K.S., Jiamg, Z.J., & Leung, P., *ApJ* **604**, 317 (2004).
- ²² Takata, J., Shibata, S., Hirotani, K., & Chang, H.-K., *MNRAS* **366**, 1310 (2006).
- ²³ Muslimov, A.G., & Harding, A.K., *ApJ* **588**, 430 (2003).
- ²⁴ Muslimov, A.G., & Harding, A.K., *ApJ* **606**, 1143 (2004).
- ²⁵ Dyks, J., Rudak, B., & Harding, A.K., *ApJ* **607**, 939 (2004).
- ²⁶ Romani, R.W., Miller, A.J., Cabrera, B., Nam, S.V., & Martinis, J.M., *ApJ* **563**, 221 (2001).
- ²⁷ Kanbach, G., Slowikowska, A., Kellner, S., & Steinle, H., *AIPC* **801**, 306 (2005).
- ²⁸ Heyl, J.S., & Shaviv, N.J., *MNRAS* **311**, 555 (2000).
- ²⁹ Silver, E.H., Weisskopf, M.C., Kestenbaum, H.L., Long, K.S., Novick, R., & Wolff, S., *ApJ* **221**, 99 (1978).
- ³⁰ Daugherty, J. K., & Harding, A. K., *ApJ* **458**, 278 (1996).
- ³¹ Romani, R. & Yadigaroglu, I.-A., *ApJ* **438**, 314 (1995).
- ³² Velusamy, T. *MNRAS* **212**, 359 (1985).
- ³³ Bietenholz, M.F., & Kronberg, P.P., *ApJ* **357**, L13 (1990).
- ³⁴ Hickson, P., & van den Bergh, S., *ApJ* **365**, 223 (1990).
- ³⁵ Michel, F.C., Scowen, P.A., Dufour, R.J., & Hester, J.J., *ApJ* **368**, 463 (1991) [Fig. D-4].
- ³⁶ Weisskopf, M.C., Hester, J.J., Tennant, A.F., Elsner, R.F., Schulz, N.S., Marshall, H.L., Karovska, M., Nichols, J.S., Swartz, D.A., Kolodziejczak, J.J., & O'Dell, S.L., *ApJ* **536**, L81 (2000).
- ³⁷ Mori, K., Burrows, D., Hester, J.J., Pavlov, G.G., Shibata, S., & Tsunemi, H., *ApJ* **609**, 186 (2004).
- ³⁸ Celotti, A. & Matt, G., *MNRAS* **268**, 451 (1994).
- ³⁹ Begelman M.C. & Sikora M., *ApJ* **322**, 650 (1987).
- ⁴⁰ Poutanen, J., *ApJS* **92**, 607 (1994).
- ⁴¹ Haardt, F., & Matt G., , *MNRAS* **261**, 346 (1993).
- ⁴² Poutanen, J., & Svensson, R., *ApJ* **470**, 249 (1996).
- ⁴³ Beloborodov, A.M., *ApJ* **496**, L105 (1998).
- ⁴⁴ Matt, G., Costa, E., Perola, C., & Piro, L., 23rd ESLAB Symposium on Two Topics in X-Ray Astronomy **2**, 991 (1989).
- ⁴⁵ Matt, G., *MNRAS* **260**, 663 (1993).
- ⁴⁶ Antonucci, R.R.J., *ARA&A* **31**, 473 (1993).
- ⁴⁷ Pineault, S., *MNRAS* **179**, 691 (1977).
- ⁴⁸ Connors, P.A., Piran, T., & Stark, R.F., *ApJ* **235**, 224 (1980).
- ⁴⁹ Dovciak, M., Karas V., & Matt, G., *MNRAS* **355**, 1005 (2004).
- ⁵⁰ Miniutti, G., Fabian, A.C., Goyder, R., & Lasenby, A.N., *MNRAS* **344**, L22 (2003).
- ⁵¹ Dovciak, M., Karas, V., & Matt, G., *AN* **327**, 993 (2006).
- ⁵² Koyama, K., Maeda, Y., Sonobe, T., Takeshima, T., Tanaka, Y., & Yamauchi, S., *PASJ* **48**, 249 (1996).
- ⁵³ Churazov, E., Sunyaev, R.A., & Sazonov, S., *MNRAS* **330**, 817 (2002).
- ⁵⁴ Weisskopf, M.C., Berthelsdorf, R., Epstein, G., Linke, R., Mitchell, D., Novick, R., & Wolff, R.S., *RvSciInstr* **43**, 967 (1972).
- ⁵⁵ Weisskopf, M.C., Cohen, C.G., Kestenbaum, H.L., Long, K.S., Novick, R., & Wolff, R.S., *ApJ* **202**, L77 (1976).
- ⁵⁶ Weisskopf, M.C., Elsner, R.F., Novick, R., Kaaret, P., & Silver, E., *SPIE* **1159**, 607 (1989).
- ⁵⁷ Weisskopf, M.C., Elsner, R.F., Novick, R., Kaaret, P., & Silver, E., *SPIE* **1343**, 457 (1990).
- ⁵⁸ Austin, R.A. & Ramsey, B.D., *OptEng* **32**, 1990 (1993).
- ⁵⁹ Costa, E., Soffitta, P., Bellazzini, R., Brez, A., Lumb, N., & Spandre, G., *Nature* **411**, 662 (2001).
- ⁶⁰ Bellazzini, R., Spandre, G., Minuti, M., Baldini, L., Brez, A., Cavalca, F., Latronico, L., Omodei, N., Massai, M.M., Sgro', C., Costa, E., Soffitta, P., Krummenacher, F., & de Oliveira, R., *NuclIM A566*, 552 (2006).
- ⁶¹ Bellazzini, R., Spandre, G., Minuti, M., Baldini, L., Brez, A., Latronico, L., Omodei, N., Massai, M., Pinchera, M., Pesce-Rollins, M., Sgro', C., Costa, E., Soffitta, P., Sipila, H., & Lempinen, E., *NuclIM A579*, 853 (2007).
- ⁶² Pacciani, L., Costa, E., Di Persio, G., Feroci, M., Soffitta, P., Baldini, L., Bellazzini, R., Brez, A., Lumb, N., & Spandre, G., *SPIE* **4843** 394 (2003).
- ⁶³ Ramsey, B.D., *AdvSpRes* **38**, Issue 12, 2985 (2006).
- ⁶⁴ Ramsey, B.D., Elsner, R.F., Engelhaupt, D.E., O'Dell, S.L., Speegle, C.O., & Weisskopf, M.C., *SPIE* **4851**, 631 (2003).
- ⁶⁵ Moretti, A., Campana, S., Lazzati, D., & Tagliaferri, G., *ApJ* **588**, 696 (2003).